Monthly Notices
of the
ROYAL ASTRONOMICAL SOCIETY

MNRAS **447,** 2575–2587 (2015) doi:10.1093/mnras/stu2600

The impact of star formation and gamma-ray burst rates at high redshift on cosmic chemical evolution and reionization

Elisabeth Vangioni,[1⋆] Keith A. Olive,[2] Tanner Prestegard,[3] Joseph Silk,[1,4] Patrick Petitjean[1] and Vuk Mandic[3]

[1]*Institut d'Astrophysique de Paris, UMR 7095 CNRS, University Pierre et Marie Curie, 98 bis Boulevard Arago, Paris F-75014, France*
[2]*William I. Fine Theoretical Physics Institute, School of Physics and Astronomy, University of Minnesota, Minneapolis, MN 55455, USA*
[3]*School of Physics and Astronomy, University of Minnesota, Minneapolis, MN 55455, USA*
[4]*Department of Physics and Astronomy, The Johns Hopkins University, Baltimore, MD 21218, USA*

Accepted 2014 December 1. Received 2014 December 1; in original form 2014 September 15

ABSTRACT

Recent observations in the total luminosity density have led to significant progress in establishing the star formation rate (SFR) at high redshift. Concurrently observed gamma-ray burst rates have also been used to extract the SFR at high redshift. The SFR in turn can be used to make a host of predictions concerning the ionization history of the Universe, the chemical abundances, and supernova rates. We compare the predictions made using a hierarchical model of cosmic chemical evolution based on three recently proposed SFRs: two based on extracting the SFR from the observed gamma-ray burst rate at high redshift, and one based on the observed galaxy luminosity function at high redshift. Using the *WMAP*/*Planck* data on the optical depth and epoch of reionization, we find that only the SFR inferred from gamma-ray burst data at high redshift suffices to allow a single mode (in the initial mass function – IMF) of star formation which extends from $z = 0$ to redshifts >10. For the case of the SFR based on the observed galaxy luminosity function, the reionization history of the Universe requires a bimodal IMF which includes at least a coeval high- (or intermediate-) mass mode of star formation at high redshift ($z > 10$). Therefore, we also consider here a more general bimodal case which includes an early-forming high-mass mode as a fourth model to test the chemical history of the Universe. We conclude that observational constraints on the global metallicity and optical depth at high redshift favour unseen faint but active star-forming galaxies as pointed out in many recent studies.

Key words: stars: abundances – stars: Population III – galaxies: star formation – dark ages, reionization, first stars.

1 INTRODUCTION

Any model of galactic or cosmic chemical evolution will depend on an assumed stellar initial mass function (IMF) and a potentially measurable star formation rate (SFR). In fact, only the convolution of the two is measurable through the observed luminosity density. Nevertheless, dramatic improvements have been made in our understanding of the star formation history, particularly at high redshift. The pioneering work of Lilly et al. (1996) using the Canada–France Redshift Survey started the path towards obtaining the comoving luminosity density at redshifts up to $z \sim 1$, quickly followed by numerous studies which showed an intense period of star formation between redshifts $1 < z < 2$ (Madau et al. 1996; Connolly et al. 1997; Madau, Pozzetti & Dickinson 1998) and up to $z \lesssim 4$ (Sawicki, Lin & Yee 1997) which showed some evidence for a downturn in the inferred SFR.

A large body of measurements of the luminosity density spanning redshifts up to $z = 6$ was compiled by Hopkins (2004) and updated in Hopkins & Beacom (2006). These results point to a sharply rising SFR at low redshifts which peaks at around $z \sim 2$ and falls off at large redshifts. The redshift range was extended in a series of papers (Bouwens et al. 2007, 2008, 2011, 2014a,b; Oesch et al. 2012, 2013, 2014a,b) which now include data out to a remarkable $z \approx 11$. The inferred fall-off of the SFR, Ψ, at $z > 8$ appears to be quite steep, $\Psi \propto (1 + z)^{-9}$ (Oesch et al. 2014a).

Le Borgne et al. (2009) had used the infrared (IR) galaxy counts to deduce the corresponding cosmic star formation history. Their

⋆E-mail: vangioni@iap.fr

study present measurements of the IR luminosity function and they concluded that a sub-population of colder galaxies exists. Recently, Madau & Dickinson (2014) have reviewed in great detail the cosmic star formation history and specifically discuss different complementary techniques which allow one to map the history of cosmic star formation. Particularly important is the correction due to dust attenuation of the far-UV luminosity density in order to be able to convert it to a SFR. One way of estimating the attenuation factor is a comparison of the uncorrected inferred far-UV and far-IR SFRs (Burgarella et al. 2013). This remains as one of the chief uncertainties in establishing the SFR at high redshift. Another issue is the contribution of emission lines to the apparent cosmic SFR density (CSFRD). However a general conclusion from the optical/UV/IR data is that the stellar mass density inferred from the CSFRD matches that observed over the entire observed redshift range (Madau & Dickinson 2014).

Recently, in an attempt to reduce systematic uncertainties induced due to the unknown stellar mass-to-halo mass relation, Markov chain Monte Carlo methods were employed on the large extant data base up to $z = 8$ (Behroozi, Wechsler & Conroy 2013). While there is certainly qualitative agreement (when normalized to the same IMF) with the earlier work of Hopkins & Beacom (2006), the new SFR of Behroozi et al. (2013) peaks at slightly lower redshift.

It is well known that there may be significant uncertainties in extracting the SFR from the luminosity function at large redshift. As noted above, this may be due to dust obscuration, but also more importantly, due to the fact that in any scenario of hierarchical structure formation, early star formation takes place in very faint galaxies (or protogalaxies) and may be missed in existing surveys which are magnitude-limited. Indeed it has been argued (Kistler, Yuksel & Hopkins 2013) that integrating the luminosity function down to $M = -10$ (significantly below the lowest measured value of $M_{\rm vis} \simeq -18$) would lead to a significant increase in the SFR at redshifts $z \gtrsim 4$. In addition, downsizing, which is both observed, (e.g. Behroozi et al. 2013; Zwart et al. 2014), and theoretically interpreted via the impact of feedback models on gas consumption (Genel et al. 2014; Schaye et al. 2015), further complicates matters.

An alternative to searching for star formation in low-luminosity galaxies is possible if we can connect the rate of gamma-ray bursts (GRBs) at high redshift to the SFR (Totani 1997; Mao & Mo 1998; Wijers et al. 1998; Porciani & Madau 2001; Bromm & Loeb 2002; Daigne, Rossi & Mochkovitch 2006a; Chary, Berger & Cowie 2007; Ishida, de Souza & Ferrara 2011). Recent attempts at making such a connection (Kistler et al. 2008, 2009, 2013; Yüksel et al. 2008; Wang & Dai 2009; Wyithe et al. 2010; Robertson & Ellis 2012; Wang et al. 2012; Wang 2013) have all indicated a higher SFR at high z relative to methods using luminosity functions. Using GRBs to trace the SFR, one would infer a much slower fall-off as a function of redshift, $\Psi \propto (1+z)^{-3}$ (Robertson & Ellis 2012; Kistler et al. 2013; Wang 2013) for $z > 4$. We note that the relation between the SFR and the GRB rates is very uncertain and the method to derive the SFR redshift evolution from GRBs includes numerous assumptions and still largely unknown biases (Vergani, private communication; see also Vergani 2013; Vergani et al. 2014). However, this is still a promising method and we will use these results as illustrative cases. Noting the systematic uncertainty in connecting the rate of GRBs with the SFR, attempts at modelling the relation have produced somewhat more moderate results for the SFR at high z (Wanderman & Piran 2010; Jimenez & Piran 2013; Trenti, Perna & Tacchella 2013; Sokolov 2014), still consistent with the lower bounds found in Kistler et al. (2013).

The choice of SFR has direct consequences on the chemical and reionization history of the Universe. A steeply falling SFR, as obtained from the luminosity density at high redshift (cf. Behroozi et al. 2013; Oesch et al. 2014a,b), is likely to be insufficient for explaining the optical depth extracted from cosmic microwave background (CMB) data (Hinshaw et al. 2013; Planck Collaboration XVI 2014a,b) and an additional high-redshift mode of star formation which can be associated with a top-heavy IMF is one way of alleviating this problem (Daigne et al. 2004, 2006b; Rollinde et al. 2009). Moreover, the early enrichment of the intergalactic medium (IGM) similarly points to an additional massive mode beyond that extracted from the luminosity function (Daigne et al. 2004, 2006b; Rollinde et al. 2009; Shull et al. 2012; Trenti et al. 2012).

In contrast, it has been argued that reionization (Gallerani et al. 2008; Wang 2013) and metal enrichment (Wang et al. 2012) may better match observations if instead the SFR implied from the GRB rate is used. This conclusion is especially apparent in the comparison of DLA data (Rafelski et al. 2012) and cluster data as compiled by Madau & Dickinson (2014), higher ionization states resulting however in smaller inferred metallicities. We note also that the specific SFR (sSFR) is in better agreement with that inferred from the CSFRD over the redshift range from 0 to 8 (Madau & Dickinson 2014), if the emission line-corrected values of Stark et al. (2013) are used.

Here, we will explore the consequences of three choices for the SFR. (1) The SFR derived from the luminosity function of faint high-redshift galaxies from Behroozi et al. (2013) supplemented with the high-redshift observations of Bouwens et al. (2011, 2014b), Oesch et al. (2012, 2013, 2014a,b). (2) The SFR implied by the Swift GRB rate from Kistler et al. (2013) and compare that to the SFR derived by Robertson & Ellis (2012) and Wang (2013). (3) An intermediate case where the SFR is scaled down by 0.3 dex, based on the models of Trenti et al. (2013), Behroozi & Silk (2014). For the normal mode of star formation which extends to the present day, we will assume a Salpeter IMF. When appropriate, we will assume a high-redshift mode of star formation which peaks at a redshift $z \gtrsim 10$. While it is generally assumed that the initial mode of star formation is massive (Bromm & Larson 2004; Bromm et al. 2009), it is possible that the high-z mode is dominated by intermediate-mass stars (Yoshii & Saio 1986; Smith et al. 2009; Safranek-Shrader, Bromm & Milosavljević 2010; Schneider & Omukai 2010). In all cases, we will work in the context of a hierarchical model for structure formation. This is coupled to a detailed model for cosmic chemical evolution (Daigne et al. 2004, 2006b; Rollinde et al. 2009), and allows us to keep track of the ionization history of the Universe, track the abundances of many of the elements produced in massive and low-/intermediate-mass stars as a function of redshift, as well as track the rate of supernovae of Type II (SNII), the sSFR, and the stellar mass density.

In the next section, we briefly describe the model of cosmic chemical evolution employed and our parametrization of the four choices of SFRs based on the Springel & Hernquist (2003) form for the SFR. For the case where an additional mode of star formation is required, we optimize the choice of the SFR by scanning the parameter space and minimizing a χ^2 likelihood function. We then compute the resulting ionization and chemical history of the Universe for each of the SFRs considered. A priori, we assume only a normal mode of star formation which extends to the present day. When this is found to be insufficient, we add a complementary high-z mode in order to achieve concordance for both the reionization and metal enrichment. The resulting chemical evolution and a

comparison of the four SFRs is given in Section 3. A discussion of our results is given in Section 4.

2 THE SFR AT HIGH REDSHIFT

Our work here is developed from a model of hierarchical structure formation based on the Press–Schechter formalism (Press & Schechter 1974) which determines the rate at which structures accrete mass. The model includes exchanges of baryonic mass between the gas within (the ISM) and exterior to (the IGM) structures. We assume a minimum mass for star-forming structures of 10^7 $M_\odot$. Details of the model can be found in Daigne et al. (2004, 2006b) and Rollinde et al. (2009).

In all cases, we assume an IMF with a single Salpeter slope ($x = 1.35$). The normal mode of star formation includes stellar masses between 0.1 and 100 $M_\odot$. When this is supplemented with a high-redshift mode, we assume a mass range of 36–100 $M_\odot$ for high-mass stars. Many studies have shown that this mass range is now preferred due to nucleosynthetic and hydrodynamical constraints (Daigne et al. 2004, 2006b; Chen et al. 2014). For a global analysis see Bromm (2013). Our SFR is always parametrized using the form given by Springel & Hernquist (2003):

$$\psi(z) = \nu \frac{a \exp(b\,(z - z_{\rm m}))}{a - b + b \exp(a\,(z - z_{\rm m}))}\,. \quad (1)$$

The amplitude (astration rate) and the redshift of the SFR maximum are given by ν and $z_{\rm m}$ respectively, while b and $b - a$ are related to its slope at low and high redshifts, respectively.

To determine the ionization history, we take the evolution of the volume-filling fraction of ionized regions to be

$$\frac{{\rm d}Q_{\rm ion}(z)}{{\rm d}z} = \frac{1}{n_{\rm b}} \frac{{\rm d}n_{\rm ion}(z)}{{\rm d}z} - \alpha_{\rm B} n_{\rm b} C(z) Q_{\rm ion}^2(z) (1+z)^3 \left|\frac{{\rm d}t}{{\rm d}z}\right|, \quad (2)$$

where $n_{\rm b}$ is the comoving density in baryons, $n_{\rm ion}(z)$ the comoving density of ionizing photons, $\alpha_{\rm B}$ the recombination coefficient, and $C(z)$ the clumping factor. This factor is taken from Greif & Bromm (2006) and varies from a value of 2 at $z \leq 20$ to a constant value of 10 for $z < 6$. ${\rm d}t/{\rm d}z$ is taken to be the standard form for a Λ-cold-dark-matter cosmology with a density of matter $\Omega_{\rm m} = 0.27$ and a density of 'dark energy' $\Omega_\Lambda = 0.73$ and taking $H_0 = 71$ km s^{-1} Mpc^{-1}. The escape fraction, $f_{\rm esc}$, is set to 0.2 for each of our assumed modes of star formation. The number of ionizing photons for massive stars is calculated using the tables given in Schaerer (2002). Finally, the Thomson optical depth is computed as in Greif & Bromm (2006):

$$\tau = c \sigma_{\rm T} n_{\rm b} \int_0^z {\rm d}z'\, Q_{\rm ion}(z') \left(1 + z'\right)^3 \left|\frac{{\rm d}t}{{\rm d}z'}\right|, \quad (3)$$

where z is the redshift of emission, and $\sigma_{\rm T}$ the Thomson scattering cross-section. The latest result for the optical depth from the Planck Collaboration XVI (2014a,b) is based on the nine-year (Hinshaw et al. 2013) polarization data and the two studies of optical depth are not substantially different. Here we use the Hinshaw et al. (2013) result of $\tau = 0.089 \pm 0.014$ to compare with model predictions.

In what follows we consider four choices for the SFR. We begin with the SFR inferred from the GRB rate (Robertson & Ellis 2012; Kistler et al. 2013; Wang 2013) which has the highest SFR at high z of the models considered (model 1). Trenti et al. (2013) argued that the normalization used to construct the SFR from the GRB rate should not evolve beyond $z = 4$ because most galaxies would have low enough metallicity that the GRB rate saturates. In fact the specific mass accretion rate from simulations can be applied to compute the SFR by assuming the empirical ratio of stellar to halo mass obtained by normalizing to data at $z \lesssim 4$, to successfully account for the observations to $z \sim 8$, and then to predict the sSFR (discussed below) and SFR, to $z \sim 15$ (Behroozi & Silk 2014). This corresponds to our second model below (model 2). The third model considered is based on the galaxy luminosity function (Behroozi et al. 2013; Bouwens et al. 2014b): model 3. We will show, however, that this model marginally fails, for reasonable escape fractions, to give sufficient CMB optical depth, and develop a variant (model 4) in which a complementary, high $z \gtrsim 10$, mode of massive star formation is added to simultaneously account for enrichment and ionization.

2.1 The SFR based on the GRB rate

Keeping in mind the uncertainties in converting the GRB rate to a global SFR, we begin by first considering the SFR obtained from the GRB rate in Kistler et al. (2013). We have fit the SFR to the Springel & Hernquist (2003) form and find $\nu = 0.145 \pm 0.006$ $M_\odot$ yr^{-1} Mpc^{-3}, $z_{\rm m} = 1.86 \pm 0.03$, $a = 2.80 \pm 0.02$, and $b = 2.62 \pm 0.02$. The χ^2 per degree of freedom for this fit is 0.51. The SFR is shown by the black curve in the left-hand panel of Fig. 1 and is chosen to fit the data from Kistler et al. (2013) represented by the five black points (with high SFR and large redshift) as well as the red points providing the bulk of the data at low redshift which are taken from Behroozi et al. (2013).[1] In order to test the effects of the GRB data on the SFR, the fit uses the low-redshift data up to redshift $z \leq 3$. At higher redshift, the significant amount of dispersion, smaller error bars, and the overlap with the GRB data would dominate the fit and minimize the effect of GRB data given the Springel & Hernquist (2003) form for the SFR which we have assumed. The slope at low z (below the peak), is determined by data compiled in Behroozi et al. (2013), and as one can see, this choice of the slope parameters fits the high-redshift data of Kistler et al. (2013) quite well. For comparison, we also show in Fig. 1(a) the GRB-based data from Robertson & Ellis (2012, blue points) and from Wang (2013, green points). The corresponding fit to the SFR determined by the Robertson & Ellis (2012) data is $\nu = 0.147 \pm 0.006$ $M_\odot$ yr^{-1} Mpc^{-3}, $z_{\rm m} = 1.78 \pm 0.03$, $a = 2.77 \pm 0.02$, and $b = 2.50 \pm 0.03$ and is shown by the blue curve. The χ^2 per degree of freedom for this fit is 0.52. The corresponding fit to the SFR determined by the Wang (2013) data is $\nu = 0.146 \pm 0.004$ $M_\odot$ yr^{-1} Mpc^{-3}, $z_{\rm m} = 1.80 \pm 0.03$, $a = 2.78 \pm 0.02$, and $b = 2.54 \pm 0.03$ and is shown by the green curve. The χ^2 per degree of freedom for this fit is 0.51. As one can see, the fits are very similar, differing primarily in the value for b which determines the slope at high redshift.

The optical depth for the GRB-based models as a function of redshift in shown by the solid black, green, and blue curves in the right-hand panel of Fig. 1 corresponding to the three sets of GRB-based data discussed above. As one can see, each case exceeds the 68 per cent CL limit of the *WMAP* result for the optical depth, τ. For these models, $\tau(z = 30) = 0.150$, 0.118, and 0.106 for the black, green, and blue curves and $z_{\rm I} = 12.47$, 10.60, and 9.84, respectively where $z_{\rm I}$ is defined as the redshift at which $Q_{\rm ion} = 0.5$. The *WMAP* value for $z_{\rm I}$ is 11.1 ± 1.1.

[1] These points have been scaled upward by a factor of 1.7 relative to the values given in Behroozi et al. (2013) to account for our choice of a Salpeter IMF (Behroozi, private communication). In Behroozi et al. (2013), the Chabrier (2003) IMF was chosen.

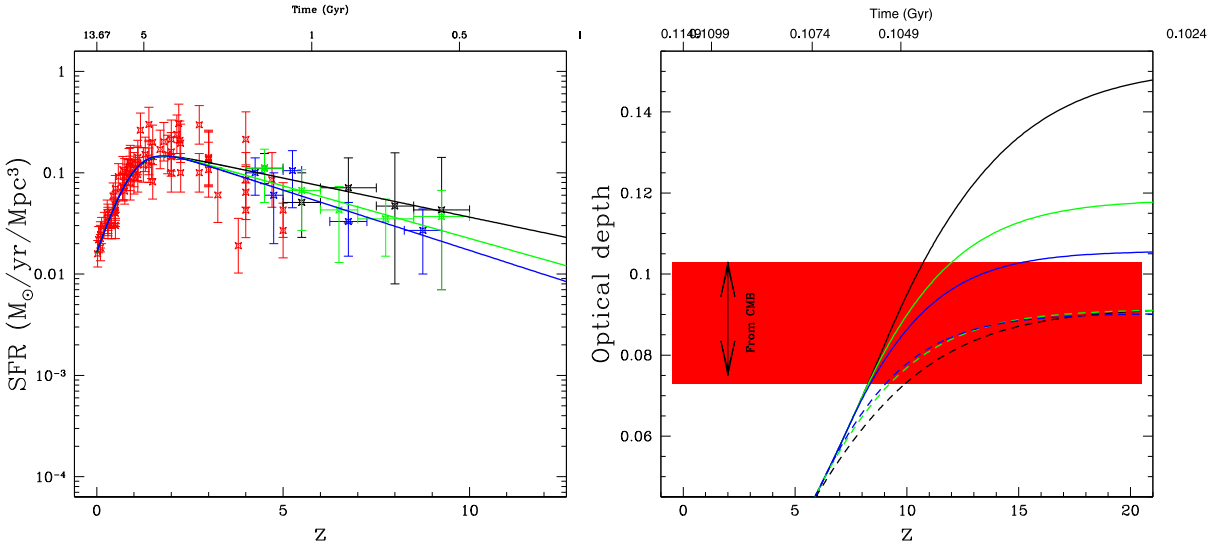

Figure 1. (a) Fit to the SFR based on the GRB rate as derived in Kistler et al. (2013) (model 1 – black curve) and compared with the SFR based on the GRB derived in Robertson & Ellis (2012, blue) and Wang (2013, green). The data and corresponding fits are colour coded; (b) the derived optical depth for the three choices of GRB based SFR's, respectively. The dashed curves assume $f_{\rm esc} = 0.05$, black, 0.12, blue, 0.09, green as opposed to $f_{\rm esc} = 0.2$ as assumed for the solid curves. All quantities are shown as functions of redshift. Observational constraints are given in the text. Note that the SFR for models 2, 3, and 4 are presented separately in Figs 3, 4, and 6 for clarity as we have used different observational constraints for the SFR in each case.

Although all three fits using GRB-based data for the SFR lead to a somewhat excessive optical depth at high redshift, this conclusion is tied to our choice for the escape fraction, $f_{\rm esc} = 0.2$. In each case, choosing a smaller value for the escape fraction would bring down the optical depth. In the right-hand panel of Fig. 1, we also show the resulting optical depth as a function of redshift for the choices $f_{\rm esc} = 0.05$, 0.09, and 0.12 for the black, green, and blue curves (shown dashed). These values of $f_{\rm esc}$ were chosen to match the central value of τ for each of the fits. However, $z_{\rm I} = 8.43$, 8.70, and 8.73 for each of the three sets of data, respectively, and all fall significantly below the *WMAP* determined value.

In Fig. 2, we show the overall metallicity relative to the solar metallicity (solid red curve in the left-hand panel) and SNII rate (solid red curve in the right-hand panel) as functions of redshift for the GRB-based data from Kistler et al. (2013).[2] In the left-hand panel of Fig. 2, observational data (black points) come from Rafelski et al. (2012). There, they present chemical metallicity measurements [*M*/H] (coming from different elements: Si, S, Zn, Fe, O) for 47 damped Lyα (DLA) systems, 30 at $z > 4$, observed with the Echellette Spectrograph and Imager and the High Resolution Echelle Spectrometer on the Keck telescopes. They combine these metallicity measurements with 195 from previous surveys, which were drawn from the SDSS-DR3 and SDSS-DR5 surveys for DLA systems performed by Prochaska, Herbert-Fort & Wolfe (2005) and Prochaska & Wolfe (2009), respectively. Moreover, we have added the nine mean points (cyan points) from Rafelski et al. (2012, see their fig. 11) where horizontal error bars are determined such that there are equal numbers of data points per redshift bin. We note that at high redshift ($z > 4$), models 1 and 2 (red lines) are a good fit to these mean *Z* observations. This could support the idea that GRBs could be better SFR tracers at high z. In a recent study, Cucchiara et al. (2014) show that the metallicity measured in DLAs associated with GRBs seems to decline at a shallower rate than the metallicity measured in DLAs associated with quasi-stellar objects (QSOs). However, we caution that the GRB-DLA may be polluted with metals from the local ongoing star-forming activity and the corresponding metallicity may not be as representative of the overall metallicity in the neutral gas as the metallicity in QSO-DLAs.

The GRB rate-inferred cosmic star formation history is anti-biased with regard to the dark matter distribution according to Jimenez & Piran (2013), who argue that the implied preference for regions of high star formation accounts for the apparent enhancement in the corresponding star formation history. This conclusion is supported by our chemical evolution study: we obtain a slope that matches the data for the GRB-inferred cosmic star formation history, and agrees in normalization if we reduce the effective yield by a factor ∼3.

In the right-hand panel of Fig. 2, data points indicating the cosmic SNII rate are available from several observational surveys (Botticella et al. 2008; Bazin et al. 2009; Graur at al. 2011; Li et al. 2011; Meleinder et al. 2011; Dahlen et al. 2012). Recently, the estimate for the local rate (now 1.5×10^{-4} events yr^{-1} Mpc^{-3}) has been increased. Mattila et al. (2012) argued that SN have been missed in optical surveys due to dust obscuration. The new higher rate at $z = 0$, is now in much better agreement with the types of models we are considering.

Both quantities (the total metallicity and SN rate) are sensitive to the assumed model of chemical evolution and can be used to discriminate between models and make reasonable parameter choices. Like the optical depth, in this case, both the metallicity and SN rate are somewhat high though acceptable. Clearly a single mode of star formation is sufficient to explain these data.

The above choices for the SFR can be considered as an upper limit. In particular, the data given in Kistler et al. (2013) were derived using a normalization of the GRB rate to the SFR based on the Hopkins & Beacom (2006) SFR. Any further flattening of the SFR at high redshift would produce a greater abundance of

[2] In all of the results which follow, we will use the Kistler et al. (2013) fit for model 1 with $f_{\rm esc} = 0.2$, as this will provide the largest contrast with the other models considered.

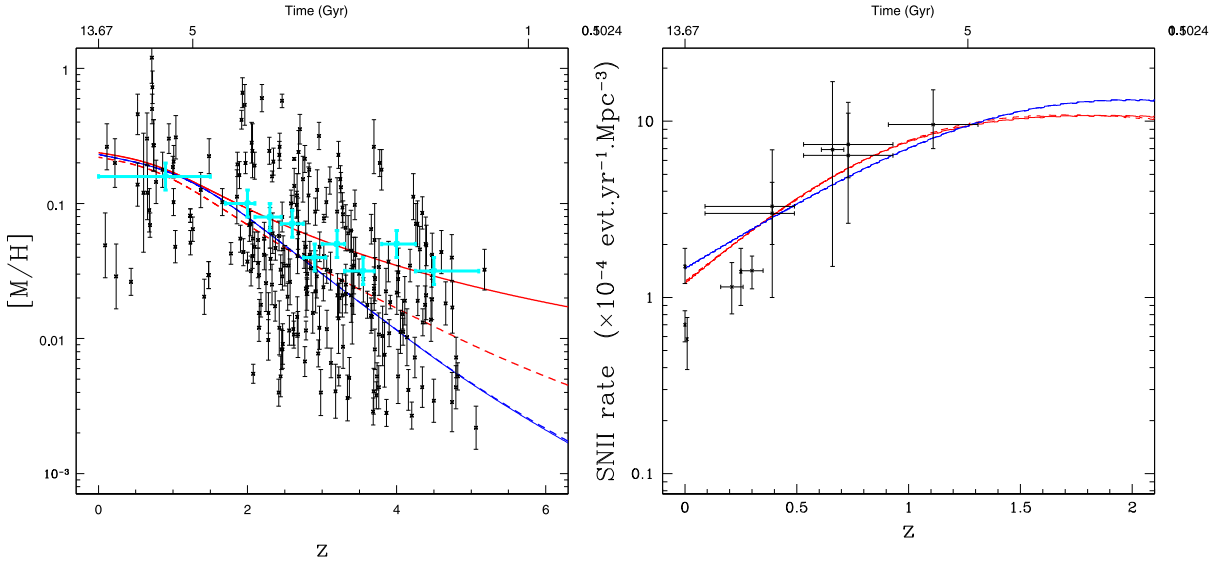

Figure 2. Left: the (log of the) metallicity abundance relative to the solar metallicity for models 1 (solid red curve), 2 (dashed red curve), 3 (solid blue curve), and 4 (dashed blue curve); right: the derived SNII rate using the same colour coding as in the left-hand panel. All quantities are shown as functions of redshift. Observational constraints are given in the text.

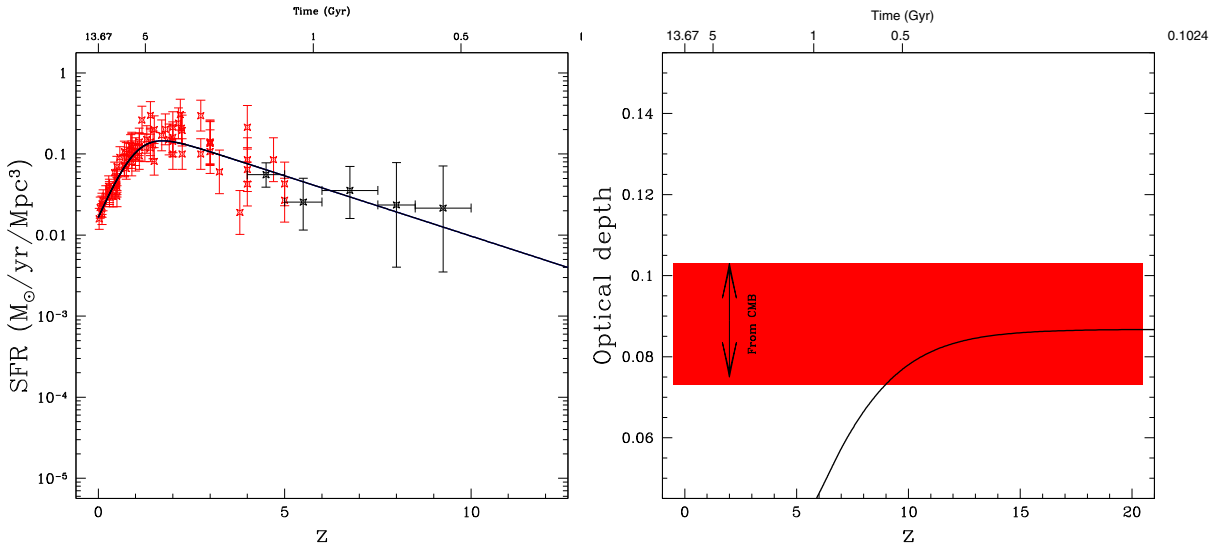

Figure 3. As in the left-hand panel of Fig. 1 the SFR for model 2, using however, the normalization derived in Behroozi et al. (2013) for the five points derived from the GRB rate, shown in black. In the right-hand panel, the corresponding optical depth.

metals and lead to an even more excessive optical depth. Adopting an alternate normalization based on the Behroozi et al. (2013) SFR leads to a lower SFR at high redshift by a factor of approximately 0.3 dex (Trenti et al. 2013; Behroozi & Silk 2014). One can obtain a more realistic SFR by assuming that two key time-scales are proportional with a fixed constant of proportionality: the inverse specific star formation and mass accretion rates. This assumption fits all data to $z \sim 8$ and has predictive power to higher $z \lesssim 15$. By a small adjustment in the slope of the SFR at high redshift, we can obtain the fit to the Behroozi et al. (2013) normalization of the SFR based on the GRB rate: $\nu = 0.146 \pm 0.006$ $M_\odot$ yr^{-1} Mpc^{-3}, $z_m = 1.72 \pm 0.03$, $a = 2.80 \pm 0.03$, and $b = 2.46 \pm 0.04$ with a χ^2 per degree of freedom of 0.52. This is shown in the left-hand panel of Fig. 3, where we now fit the five black data points which are scaled down from the five points from Kistler et al. (2013) shown in Fig. 1(a). The corresponding evolution of the optical depth is shown by the black curve in the right-hand panel of Fig. 3. We now obtain a significantly better fit for the optical depth, $\tau = 0.087$ using $f_{esc} = 0.2$, though the redshift of reionization remains somewhat low, $z_I = 8.62$. The metallicity and SNII rate in this case is very similar to that in model 1, as seen by comparing the red solid and dashed curves in the lower panels of Figs 2(a) and (b).

2.2 The SFR based on the observations of star-forming galaxies

The most conservative approach in obtaining the average SFR at high redshift comes from the direct observation of the galaxy luminosity function which yields the volume density of galaxies as a function of luminosity. Over the last 10–15 years, the data on the luminosity function have been extended out to high redshift with the most recent data reaching $z \sim 8$–10 (Oesch et al. 2014a,b; for

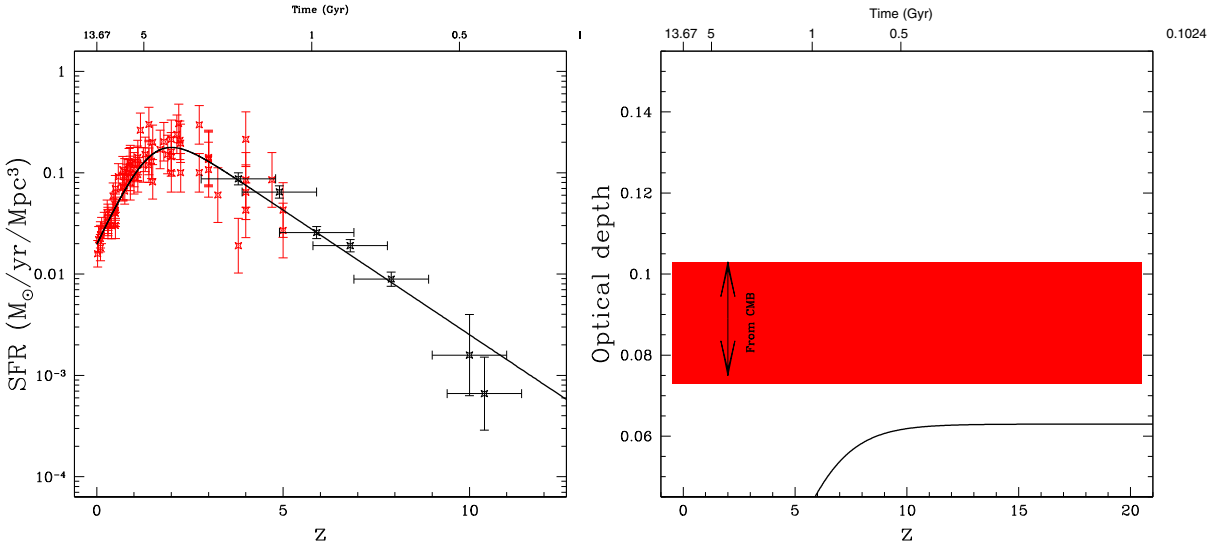

Figure 4. As in the left-hand panel of Fig. 1 using the SFR from Behroozi et al. (2013, which includes points from Bouwens et al. 2014b and Oesch et al. 2014a shown in black) from high-z observations of the luminosity function (model 3). In the right-hand panel, the corresponding optical depth.

a comprehensive discussion of these observational advances, see Bouwens et al. 2014b). Extracting the SFR, however, requires some knowledge of the halo mass function and in particular the ratio of the total stellar mass to halo mass at high redshift. Here we adopt the results of the recent analysis in Behroozi et al. (2013) where semi-analytical models of cosmological volumes were used to perform abundance matching with the galaxy luminosity function data to high z and to extract the halo star formation efficiency. A key conclusion is that stellar mass efficiency increases beyond $z \sim 4$, otherwise one would have too little stellar mass or SFR associated with galaxies at $z \sim 8$. Other studies reach similar conclusions (Trenti et al. 2010; Wyithe, Loeb & Oesch 2014).

Fitting the Springel & Hernquist (2003) form given in equation (1) to the SFR derived by Behroozi et al. (2013), we find $\nu = 0.178 \pm 0.06$ M$_\odot$ yr^{-1} Mpc^{-3}, $z_m = 2.00 \pm 0.04$, $a = 2.37 \pm 0.02$, and $b = 1.80 \pm 0.02$ with a χ^2 per degree of freedom of 0.76. Though the parameter values used here appear similar to those used in Section 2.1 above, the part of the SFR which is of most interest here is that at large redshift, where the SFR goes as $e^{(b-a)z}$ and thus declines much more rapidly in this case. This SFR is shown in the left-hand panel of Fig. 4. As one can see by the solid curve in the right-hand panel of Fig. 4, using only a single mode of star formation in this case is not sufficient to account for the optical depth derived from CMB data. For this choice of the SFR, the optical depth only rises to $\tau \approx 0.063$ at high redshift, about 2σ below the CMB value. Furthermore, the redshift of reionization is significantly below the *WMAP* value. For this case, we find $z_I = 7.02$ and is close to 4σ too low. Nevertheless, the overall metallicity and SNII rate are quite consistent with observations as seen by the solid blue curves in the lower panels of Figs 2(a) and (b). Thus in this case, we are led to consider a high-mass mode of star formation operating predominantly at high redshift, to fit the optical depth.

For the high-mass mode, we assume an IMF with a Salpeter slope (as we have done for all other IMFs) but with a restricted mass range from 36–100 M$_\odot$. Although we also use the Springel & Hernquist (2003) form for the SFR, there is now, in principle, considerable freedom for the selection of the four SFR parameters. To help in this choice we performed a scan of the 4D parameter space to minimize a χ^2 function which is described below. We include several constraints in establishing the χ^2 function:

(i) *The optical depth*: we include two contributions to χ^2 based on obtaining the correct value for the optical depth at high redshift (here taken to be $z = 30$). We use the *WMAP* value of $\tau = 0.089 \pm 0.014$. We also take in account the redshift of reionization, z_I, defined as $Q_{ion} = 0.5$. We take $z_I = 11.1 \pm 1.1$. Note that this value depends on the assumption that the Universe was reionized instantaneously from the neutral state to the fully ionized state at reionization z. In addition, the reionization history is assumed as a hyperbolic-tangent function.

(ii) *The overall metallicity*: because of the considerable amount of scatter in the metallicity data at high redshift, we use an approximate mean of the observed data with a generous uncertainty. The main goal is to insure that the computed metallicity is in the right ballpark. We compute the overall metallicity, Z, at redshifts $z = 4$ and 0. We have taken the observed values $Z(4) = 0.03 \pm 0.01$ and $Z(0) = 0.5 \pm 0.5$. Units for Z are taken to be relative to the solar metallicity.

(iii) *Individual element abundances*: the global metallicity is not sufficient for breaking inherent degeneracies in the parameter space and therefore we include as constraints the abundances of carbon and oxygen compared to the high-redshift data taken from the SAGA DataBase – Stellar Abundances for the Galactic Archaeology (Suda et al. 2008, 2011) – for roughly 140 objects for each element. The redshift for each observable is converted within the hierarchical model from the observed iron abundance.

(iv) *The SFR at high redshift:* we also include as a constraint the observed SFR at redshifts $z \approx 6$–10 comprising of five data points at the highest z from Bouwens et al. (2014b) and Oesch et al. (2014a).

The χ^2 function is then defined by taking the difference between a computed value and the data (squared) and weighted by an observational uncertainty.

Some results of the frequentist likelihood analysis are shown in Fig. 5 where we show 2D parameter planes in ν, z_m (left), and a, b (right) for the high-mass mode parameters. In the left-hand panel, we have divided the 2D ν, z_m parameter space into a 25 by 25 grid and minimized the χ^2 in each bin using a Nelder–Mead

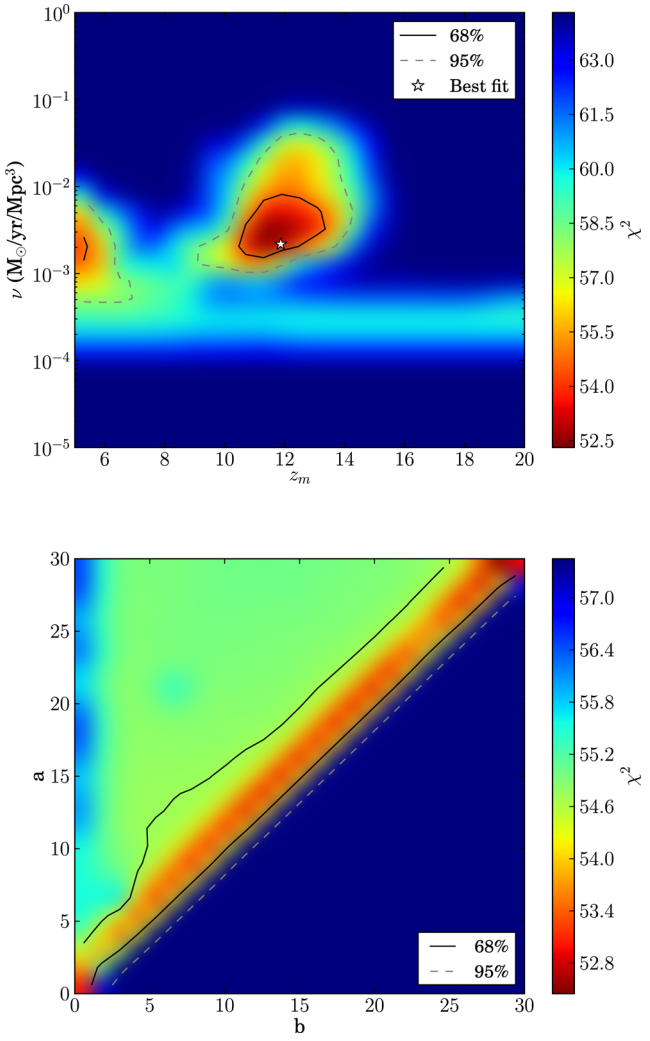

Figure 5. (a) 2D maps of χ^2 in the ν, z_m parameter plane (upper) and a, b parameter plane (lower). 68 per cent (solid) and 95 per cent (dashed) frequentist confidence intervals are shown, calculated using $\Delta\chi^2$ values of 2.30 and 5.99, respectively. The location of the best-fitting point in the upper panel is shown by a star. In the lower panel, the χ^2 is nearly constant along the diagonal $a \gtrsim b$.

simplex method (Nelder & Mead 1965). ν and z_m are not strictly fixed, but are allowed to vary within the boundaries of each bin; the other two parameters, a and b, are allowed to vary between 0 and 30. These boundaries have proved sufficient to fully explore the areas of minimal χ^2 within the model parameter space. The 68 and 95 per cent frequentist confidence intervals are calculated about the minimum χ^2 value, using $\Delta\chi^2$ values of 2.30 and 5.99, respectively (based on a χ^2 distribution with two degrees of freedom). The same procedure is repeated in the 2D a, b parameter space, allowing ν and z_m to vary between 10^{-5} and 1 $M_\odot$ yr^{-1} Mpc^{-3} and 5 and 20, respectively.

Because the normal mode of star formation is already a good fit to the SFR, we expect the high-mass mode to be rather strongly peaked at high redshift. Due to the nature of the above constraints (contributions to χ^2) we can deduce that the peak of the high-mass mode will occur near $z = 11$ so as to ensure the correct epoch of reionization. The evolution of the individual elements such as C and O serve as a limiting factor in the astration rate, ν, as there is no direct constraint available from the SFR itself. As one can see in the upper panel of Fig. 5, the χ^2 function increases very rapidly as ν is decreased below 10^{-3} $M_\odot$ yr^{-1} Mpc^{-3}. At smaller ν, the contribution of the high-mass mode becomes insignificant.

The best fit lies slightly above the 68 per cent contour as is indicated by a star. The best fit occurs at $\nu = 0.00218^{+0.38}_{-0.03}$ $M_\odot$ yr^{-1} Mpc^{-3}, $z_m = 11.87^{+0.07}_{-0.99}$. As one can see in the lower panel of Fig. 5, the χ^2 likelihood function is extremely flat along the line where $a \gtrsim b$ and the best fit has $a = 13.81$, and $b = 13.36$ (there is no useful uncertainty on the individual parameters, but as one can see from the figure the difference between a and b must be relatively small). The large values of the slope parameters a and b, lead to a sharply peaked SFR for the high-mass mode. Note that there is a second region at $z_m \lesssim 6$ in the ν, z_m plane with a reduced χ^2. In this region, there is some improvement to oxygen abundances at the expense of a reionization redshift which is too low. In that region the values of a and b are small (order 1), and the high-mass mode extends to large redshift. It is interesting to note that an extended high-mass mode peaked at relatively low redshift had been considered (Schneider et al. 2010; Tornatore, Ferrara & Schneider 2007). The horizontal feature seen in the upper panel corresponds to the limit where $a = b$ and the SFR becomes a constant equal to ν.

Adopting the best-fitting value for the parameters, we find the SFRs shown in left-hand panel of Fig. 6. The black curve is the same as in model 3 (shown in Fig. 4), the blue curve corresponds to the high-mass model (model 4). As one can see, the high-mass mode contributes very little to the SFR at $z \lesssim 10$ where data are available and is sharply peaked at $z \approx 11$.

In the right-hand panel of Fig. 6, we show the two optical depth curves as a function of redshift. The solid curve is the same as shown in Fig. 4(b), the blue line corresponds to model 4 which includes the high-mass mode. In the latter case, $\tau = 0.092$ and $z_I = 11.5$ in almost perfect agreement with the *WMAP* value for z_I. At the redshifts shown in the panels of Fig. 2 there is virtually no difference in the metallicity and SNII rates between models 3 and 4.

3 RESULTING CHEMICAL EVOLUTION

Having laid out our selection of models for the SFR, we are now in a position to explore the consequences for chemical evolution. In particular we will be interested in the evolution of the abundances of several elements. In order to compute the element abundances, we utilize mass and metallicity-dependent yields taken from the tables of yields from Woosley & Weaver (1995) for massive stars ($10 < M/M_\odot < 40$). An interpolation is made between the different metallicities (Z=0, 0.0001 $Z_\odot$, 0.001 $Z_\odot$, 0.1 $Z_\odot$, and $Z_\odot$) and we extrapolate the tabulated values beyond 40 $M_\odot$.

Our numerical results can now be compared to various observations for each element under consideration. Iron (shown in Fig. 7) is measured in DLA systems as a function of redshift. As noted earlier, when discussing the overall metallicity, most of the high-z iron data points (47) come from Rafelski et al. (2012) and 195 others from previous surveys (Prochaska et al. 2005; Prochaska & Wolfe 2009). Note that the iron abundances measured by Rafelski et al. (2012) are measured in the gas phase. It is well known that iron is depleted on to dust grains in the interstellar medium. Therefore these measurements should be considered as lower limits.

Concerning the α elements: carbon, oxygen, magnesium, and nitrogen (shown in Figs 8, 9, and 10), the data points come from the SAGA DataBase (Suda et al. 2008, 2011). In this compilation

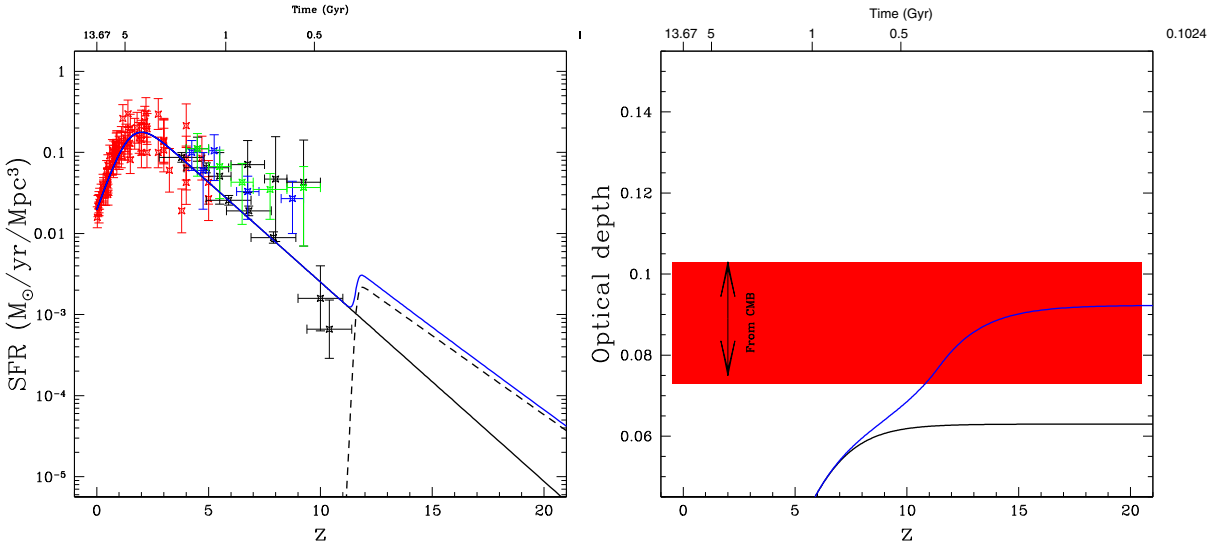

Figure 6. As in Fig. 4 with the addition of high-mass mode. In the left-hand panel, the dashed black curve corresponds to the best fit for the high-mass mode. The blue solid line corresponds to the total SFR (model 4). The corresponding optical depth is shown in the right-hand panel. The solid black line is taken from Fig. 4, the blue line corresponds to the optical depth of the total SFR.

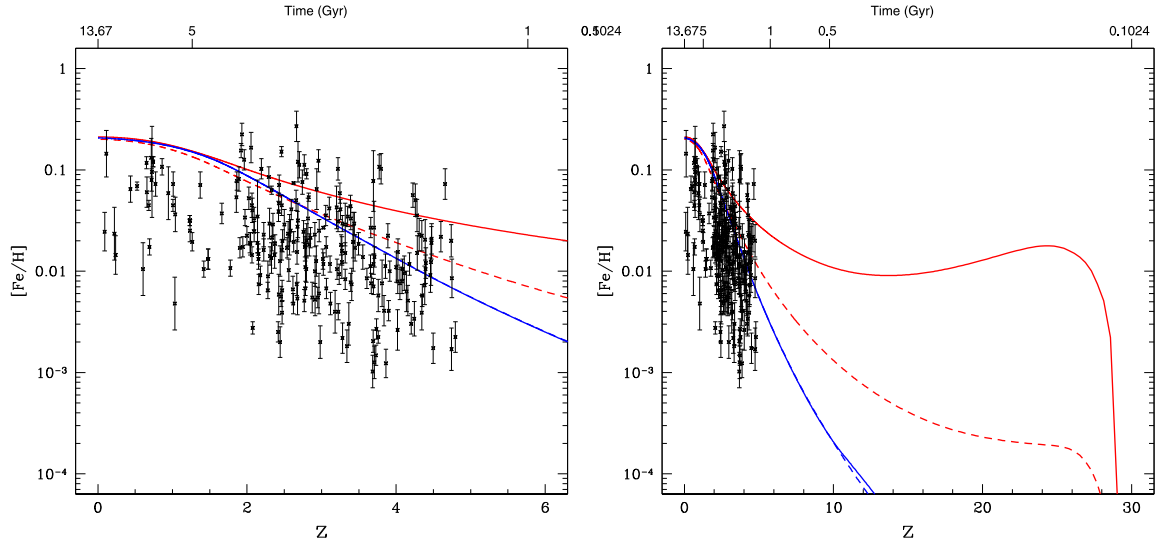

Figure 7. The evolution of the iron abundance as a function of redshift for the four models under consideration. Numerical results are compared to iron observations. These values are measured in DLA systems as a function of redshift. Most of the high-z iron data points (47) come from Rafelski et al. (2012) and 195 others from previous surveys (Prochaska et al. 2005; Prochaska & Wolfe 2009).

we have selected the bulk of standard observations (blue points corresponding to dwarfs, red and green ones to metal poor dwarfs and giant stars, respectively, and magenta points represent the ultra metal poor stars).

For each quantity, we will compare the resulting evolution using four different assumed SFRs based on: (1) the GRB rate from Kistler et al. (2013) – model 1; (2) the renormalized rate from Behroozi & Silk (2014) – model 2; (3) the observation of star-forming galaxies from Behroozi et al. (2013) without a high-mass mode – model 3; (4) the same with a high-mass mode as discussed above – model 4.

We begin the discussion with the evolution of iron. In Fig. 7, we show the evolution of the iron abundance ([Fe/H] corresponds to the log of the ratio of iron H relative to the solar ratio) as a function of redshift for the four models under consideration. The two upper curves, shown in red, correspond to the SFR based on the GRB rate (models 1 and 2). Not surprisingly, they show the highest iron abundance at any redshift. The dashed of the two corresponds to the lower normalization argued in Behroozi & Silk (2014, model 2). Moreover, we also show the iron evolution in the range 0–30 making it clear that in model 1 the iron production at high z is very high compared with the other models due to the flat slope of the SFR in model 1. The lower two curves, shown in blue (models 3 and 4), correspond to the SFR based on the luminosity function, with (dashed – model 4) and without (solid – model 3) the high-mass mode. These too, are essentially indistinguishable because the Pop III star mode is effectively efficient only at very high redshift. Recall, as noted above, these iron measurements should be considered as lower limits.

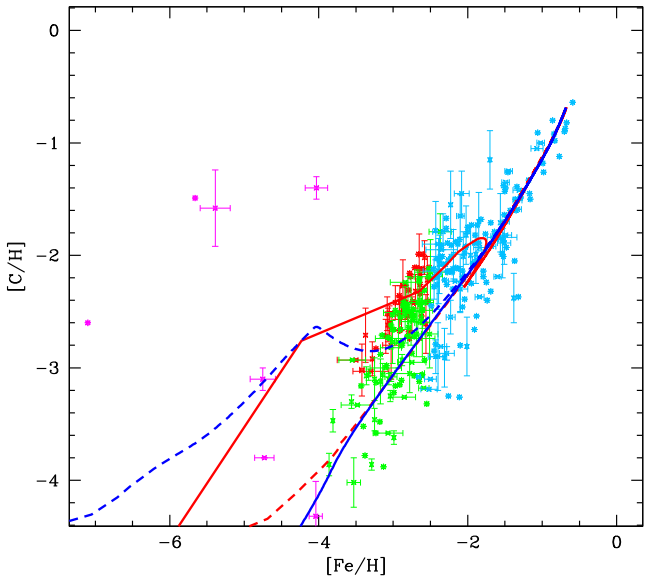

Figure 8. The evolution of the carbon abundance as a function of the iron abundance for the four models under consideration. Carbon data points come from the SAGA DataBase (Suda et al. 2008, 2011). In this compilation we have selected the bulk of standard observations, blue points corresponding to dwarfs, red and green ones to metal poor dwarfs and giant stars, respectively, and magenta points represent the ultra metal poor stars.

While one could argue that the luminosity-based SFR provides a better fit to the data, it must be noted that (i) the mean metallicity weighted by the H I column density derived by Rafelski et al. (2012) lies between the blue and red curves at any redshift and (ii) the slope of the observed evolution is closer to that of the GRB-based models so that these models may better represent reality at higher redshift.

We next consider the evolution of carbon. In Fig. 8, we show the evolution [C/H] as a function of the iron abundance for the four models under consideration. As one can see for the figures, the carbon abundance is essentially independent of our choice of model for [Fe/H] > -2 or $z < 4$. At higher z (lower metallicity), model 4 actually does a better job at an explanation of the ultra metal poor carbon enhanced metal poor (CEMP) stars, though as one can see there is considerable dispersion in these points (shown in magenta). We have not considered these in detail here as a specific study including an intermediate-mass stellar mode would be required. Thus, in this context, the carbon evolution we display is only a lower limit at very low metallicity. Note that model 1 shows a peculiar C evolution which is related to its enhanced iron evolution at high redshift. It is an intermediate case between models 2/3 and 4.

In Fig. 9, we show the analogous evolution of nitrogen and oxygen as a function of [Fe/H]. The nitrogen abundances are very similar for all four models considered. They all slightly underproduce [N/H]. Note however, that our predictions are closer to the measurements in DLA systems (Petitjean, Ledoux & Srianand 2008; Pettini et al. 2008; Zafar et al. 2014) for which [N/O] ~ -1 for [O/H] in the range between -1 and -3.

Nitrogen has different nucleosynthetic origins (compared to oxygen for example), including one from a potential intermediate-mass stellar mode which is not considered here. Consequently, our calculation provides only a lower limit to the production of nitrogen. To have an idea of how much additional N production is necessary to match the data, we have multiplied the N yield by a factor of 4 and show the result for model 4 by the dotted blue curve. In contrast to C and O, N is not produced in massive stars, so model 4 does not show a bump at low metallicity. As noted above, the consequence of the flat SFR slope in model 1 is a peculiar element evolution which cannot easily fit observational data.

The oxygen abundances for models 2 and 3 all look similar, however, the evolution of [O/H] is somewhat different for model 1 and significantly different for model 4. Here we see directly the impact of the high-mass mode which shows a local peak in [O/H] at [Fe/H] ≈ -4.8. This is the only model that can explain the abundances seen in very low metallicity stars (magenta points), as is the case for carbon as well. Due to uncertainties concerning the oxygen synthesis in massive stars, we show the [O/H] abundance for model 4 using an O yield enhancement of a factor of 2 (shown by the dotted blue curve). The result for the other models would scale similarly and provide a better fit to the data at [Fe/H] > -2.

As in the case for oxygen, the evolution of magnesium shows the impact of the high-mass mode in model 4 as seen in Fig. 10 (left) where the evolution of [Mg/H] is shown as a function of the iron abundance. While models 1, 2, and 3 all fit the data nicely, model 4 appears to overproduce Mg at [Fe/H] < -3. Once again,

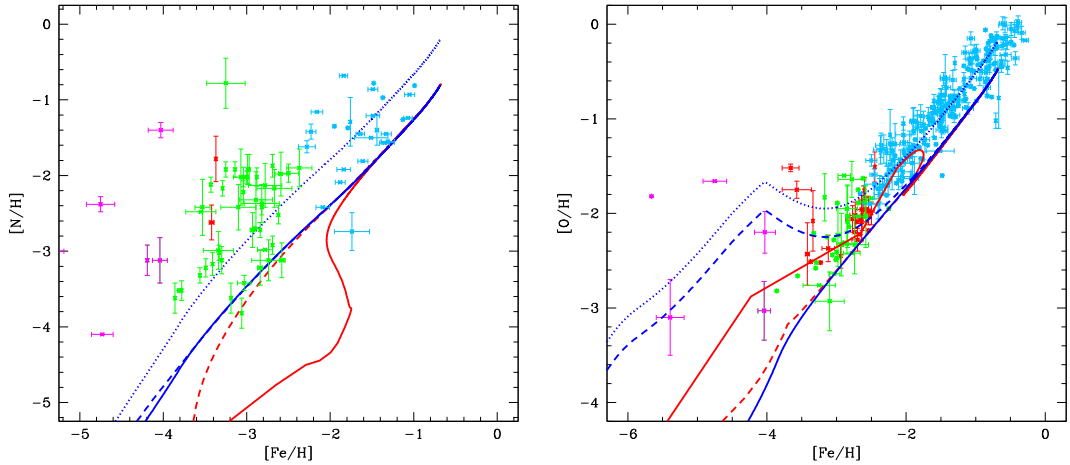

Figure 9. The evolution of the nitrogen (left) and oxygen (right) abundances as a function of the iron abundance for the four models under consideration. The blue dotted curves show the evolution of N and O using an alternate set of enhanced yields in the case of model 4. Nitrogen and oxygen data points come from the SAGA DataBase (Suda et al. 2008, 2011).

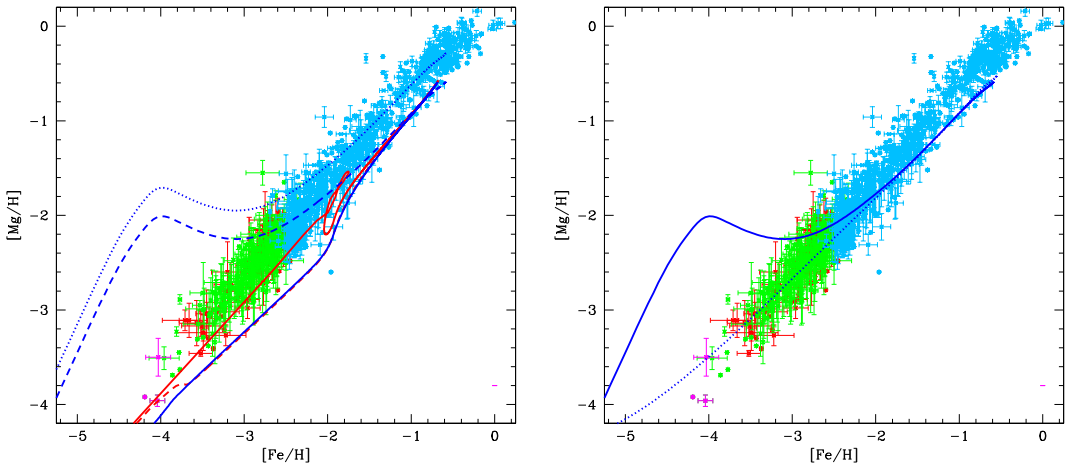

Figure 10. As in Fig. 9, the evolution of the magnesium abundance as a function of the iron abundance for the four models under consideration. In the left-hand panel, we use a Mg yield coming from Woosley & Weaver (1995). The blue dotted curve shows the evolution of Mg using an alternate enhanced yield in the case of model 4, multiplying the yield by a factor 2. In the right-hand panel, we use another yield, coming from Heger & Woosley (2010, blue dotted line) compared with the result from model 4 (solid blue line). Magnesium data points come from the SAGA DataBase (Suda et al. 2008, 2011).

for comparison, we have plotted (dotted blue line) the Mg evolution multiplying the Mg yield by a factor 2. A recent study (Heger & Woosley 2010) devoted to nucleosynthesis in massive stars at zero metallicity presents new Mg yields. There, it was found that no Mg is produced for massive stars larger than 30 $M_\odot$ in the most of the models considered at zero metallicity. We have included these new yields at very low metallicity ($Z < 0.0001\ Z_\odot$) which should result in another possible Mg production. The right-hand panel presents the Mg evolution for model 4 (which includes a massive mode at high redshift) with these two different yields: from Woosley & Weaver (1995, solid line) and from Heger & Woosley (2010, dotted line). This choice of yields for the early production of Mg provides us with another limit to Mg/H and fits the bulk of data.

A signature of a high-mass mode which corresponds to a distinct population of stars (Pop III) is clearly of great importance in understanding the chemical evolutionary history of the universe. Frebel, Johnson & Bromm (2007) defined a transition discriminant, $D_{\rm trans}$, based on the carbon and oxygen abundances at low metallicity, and recently Frebel & Norris (2013) have provided an updated formula for $D_{\rm trans}$:

$$D_{\rm trans} \equiv \log_{10}(10^{[\rm C/H]} + 0.9 \times 10^{[\rm O/H]}), \quad (4)$$

which we use here. When sufficiently abundant, ionized carbon and neutral atomic oxygen act as a trigger to lower mass star formation and signify the transition to Pop I/II star formation (Bromm & Loeb 2003; Yoshida, Bromm & Hernquist 2004). For a more detailed discussion of this quantity in the context of chemical evolution with hierarchical structure formation, see Rollinde et al. (2009).

In Fig. 11, we show the evolution of $D_{\rm trans}$ as a function of [Fe/H] for the four models. All models make similar predictions for [Fe/H] $\gtrsim -3$. Only model 4 can explain the two observations with relatively high $D_{\rm trans}$ at [Fe/H] $\lesssim -5$, while none of the models can account for the scattering of points with $D_{\rm trans}$ $\gtrsim -1$ and $-3 <$ [Fe/H] < -1. Model 1 is again an intermediate case. As noted earlier, we do not consider here the effects of an intermediate-mass mode which would be a large contributor of carbon at low metallicity. These points correspond precisely to the high C content in CEMP stars.

Finally, Fig. 12 (left) shows the evolution of the mean sSFR as a function of redshift for the four considered models. The sSFR is

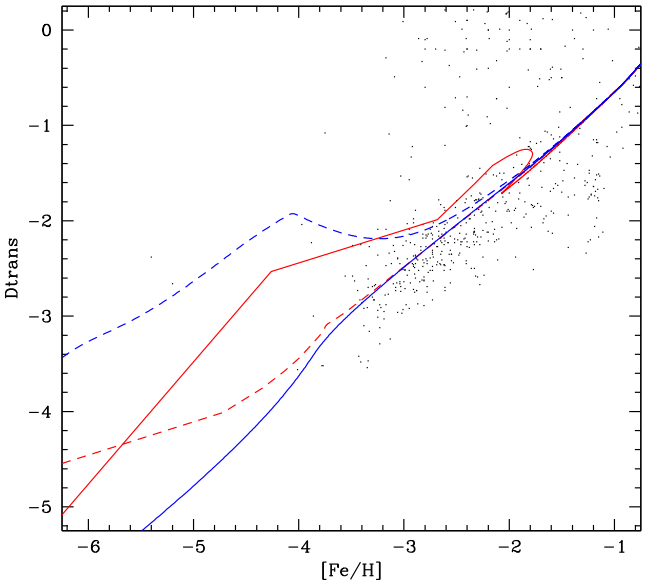

Figure 11. The evolution of the $D_{\rm trans}$ as a function of the iron abundance for the four models under consideration.

calculated by dividing the CSFRD by the mean stellar mass density (shown in the right-hand panel of Fig. 12). We have taken the compilation of data from Madau & Dickinson (2014) and added a point from Oesch et al. (2014a) at $z = 10$. The estimated stellar mass range is $10^{9.4}$–10^{10} $M_\odot$. There is no significant difference between the models. At high redshift, they fit the data points.

As usual, at low redshift, the sSFR calculation is too steep relative to data, possibly due to an overestimate of the stellar mass. The model rise from the present epoch to the $z \sim 2$ SFR peak is shallower than found in the data. It is likely that this is due to hidden star formation in dense molecular gas and the galaxy merger contribution, not included in our simple modelling and reflected in the strong difference between the SFR contributions by normal star-forming galaxies (relatively shallow and with low sSFR) and luminous IR galaxies (very steep and high sSFR) as found by Le Borgne et al. (2009).

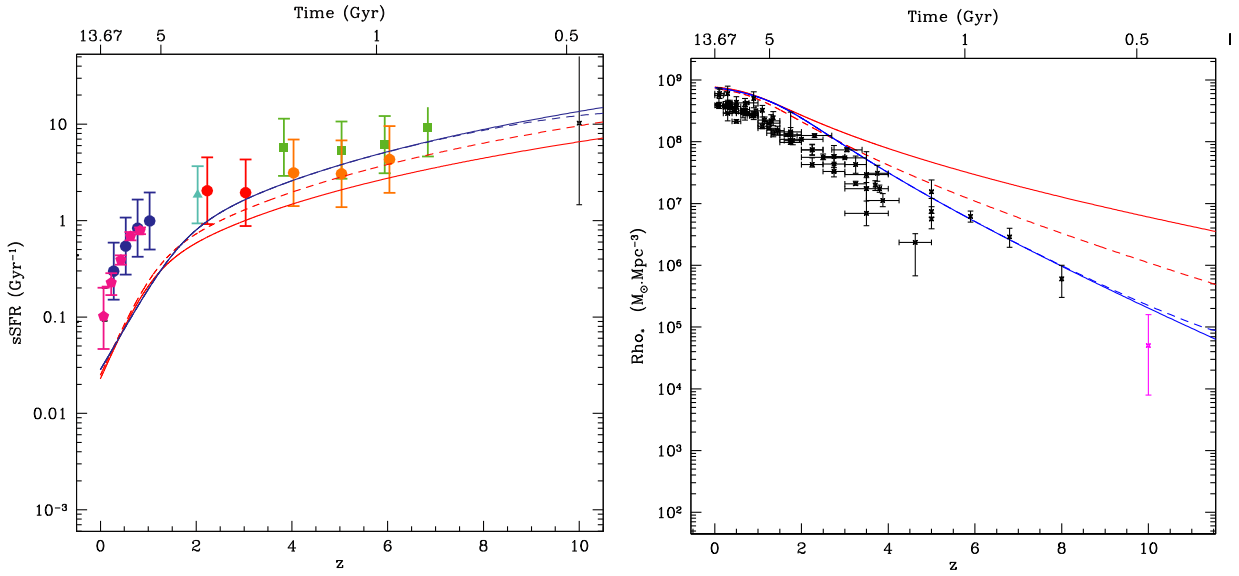

Figure 12. (a) The evolution of the mean sSFR as a function of the redshift for the four models under consideration. Stellar mass of galaxies are in the range of $10^{9.4}$–10^{10} $M_{\odot}$. Data points come from the literature (Daddi et al. 2007; Noeske et al. 2007; Damen et al. 2009; Reddy et al. 2012; Stark et al. 2013; González et al. 2014) and have been compiled in Madau & Dickinson (2014). The $z = 10$ data point comes from Oesch et al. (2014a). (b) The evolution of stellar mass density as a function of the redshift for the four models under consideration is also shown. The data points are taken from a compilation made by Madau & Dickinson (2014, their table 2) using UV and IR data. The magenta $z = 10$ data point comes from Oesch et al. (2014a).

The right-hand panel shows the evolution of the mean stellar mass density as a function of redshift. The data points are taken from the compilation by Madau & Dickinson (2014), once again adding the $z = 10$ point from Oesch et al. (2014a). Models 3 and 4 fit the observational data at high redshift. Indeed, these results clearly show the limitation of this approach at low redshift. This is related to feedback processes that prevent stars from forming and enhancing the sSFR. Models 1 and 2 cannot fit this data because these latter observations are deduced from the SFR data from observations of star-forming galaxies. While GRBs are associated with dwarf galaxies, however even just considering the data based on the GRB rate, additional dwarf galaxies are still required that are well below the observational limits. Possibly these might be associated with GRBs that have no apparent host galaxy.

4 DISCUSSION

The DLA abundances reflect enhanced SFRs at high redshift as does the intercluster medium at low redshift. The fact that these data are consistent over a wide redshift range argues against a systematic change in the IMF, but favours a dwarf galaxy population that has a steep luminosity function and hosts the GRBs. Evidence for a steep luminosity function comes both locally from dwarf galaxy surveys in clusters (Popesso et al. 2006), where harassment is thought to be responsible, and at high redshift where studies of the stellar mass function show that the faint-end slope, α, steepens from $\sim$1.6 to $\sim$2.0 over $z \sim 4$–10 (Bouwens et al. 2014b; Duncan et al. 2014), the explanation in this case presumably being due to the expected convergence to the halo mass function. The steep value of α has been found via a lensed sample of high-redshift ($z \sim 7$–8) galaxies to extend to below $0.1L^{\star}$ (Atek et al. 2014).

WMAP and *Planck* data (Hinshaw et al. 2013; Planck Collaboration XVI 2014a,b) have given us unprecedented precision in determining cosmological observables. Among these are the integrated optical depth and the corresponding epoch of reionization at $z \approx 11$. We therefore know that some stellar activity and hence chemical evolution must have taken place at a still higher redshift (assuming that stellar light is the source of reionization). The discovery of Lyman-break galaxies at $z > 3$ (Steidel et al. 1996) opened the door to a host of rest-frame UV observations of galaxies at ever increasing redshift. There are now six candidate galaxies at $z \sim 10$ (Bouwens et al. 2014b), and between 200–500 galaxies at redshift $z \sim 7$–8 (Bouwens et al. 2011; Finkelstein et al. 2012; McLure et al. 2013) allowing one to map out the global UV luminosity function and gain insight into the global SFR density. However because observations at $z \sim 10$ and above remain sparse, significant uncertainties remain in the SFR at high redshift. To some extent, the SFR determined from the galaxy luminosity function can be thought of as setting a lower limit as systematic effects due to dust obscuration would tend to increase the derived SFR. There is also the problem that such surveys are flux-limited and hence biased by the brightest galaxies, and again the true SFR might be higher, particularly at high redshift (Trenti et al. 2010; Wyithe et al. 2014). Indeed, as we have shown above (in our discussion of model 3), the SFR derived from these flux-limited surveys is not sufficient to reionize the universe at sufficiently high redshift. A similar conclusion was reached in Robertson et al. (2013).

While the true SFR may be somewhat higher at large z than that derived by the UV galaxy luminosity function, it is also possible that there was a burst of star formation at $z \approx 11$ that was primarily responsible for the reionization of the Universe. Here we have considered in model 4, the effect of such a burst on the chemical history of the Universe.

On the other hand, GRBs are expected to be visible out to very high redshifts of $z \sim 15$–20 (Lamb & Reichart 2000), the current record being $z \sim 8.2$ (Tanvir et al. 2009). Some GRBs have been associated with observed SN (Hjorth et al. 2003; Stanek et al. 2003). For a global review see Woosley & Bloom (2006). As the origin of GRBs is expected to be core collapse SN, it is sensible to infer that these events may trace the SFR as many authors have assumed. However, as discussed above, a straight fit to the SFR derived from existing GRB data would lead to an optical depth in excess of that

determined from CMB data. Extracting the SFR from GRB is also not free from its own set of uncertainties and biases (Trenti et al. 2013). Models attempting to overcome these problems predict a steeper fall-off at high redshift (Trenti et al. 2013; Behroozi & Silk 2014) and these 'softened' SFRs yield predictions for the optical depth and reionization which are quite consistent with data as we have shown in model 2.

Presently, most observations of chemical abundances are available only at relatively low redshift. For redshifts $z \gtrsim 5$, we would require observations of objects with iron abundances $[\mathrm{Fe/H}] \lesssim -3$ (see Fig. 7). Furthermore, in the hierarchical picture of structure formation which is at the core of our cosmic chemical evolution models, element abundances are primarily sensitive to the late-time SFR where the models are constrained by the low-z determination of the SFR. As a consequence, in most cases, the models considered predict very similar abundances for $[\mathrm{Fe/H}] \gtrsim -3$. Differences begin to occur at lower metallicity, and these are most apparent for model 4 where a high-mass mode of star formation is included at high redshift. Most notably this model predicts enhanced abundances of C, O, and Mg at very low metallicity as is seen in some of the most primitive stars in our own Galaxy.

It is clear that enhancement of the SFR occurs relative to that inferred from the galaxy luminosity function. This may be because faint but star-forming galaxies have been missed (as must be supposed if the GRB data is a better indicator of the true SFR), or because Pop III star formation included at high redshift results in an exclusively high-mass (and short-lived) mode of star formation. At lower redshifts, the SFRs in all models are similar (as there is far less uncertainty) and chemical abundances are far less discriminating. To better disentangle the SFR at high redshift, new abundance data is required at very low metallicity.

ACKNOWLEDGEMENTS

This work has been carried out at the ILP LABEX (under reference ANR-10-LABX-63) supported by French state funds managed by the ANR within the Investissements d'Avenir programme under reference ANR-11-IDEX-0004-02. It was also sponsored by the French Agence Nationale pour la Recherche (ANR) via the grant VACOUL (ANR-2010-Blan-0510-01). EV warmly thanks Damien Le Borgne for continuing and fruitful discussions. We also thank Yohann Dubois and Christophe Pichon for their friendly help. The work of KAO was supported in part by DOE grant DE-SC0011842 at the University of Minnesota. The work of TP and VM was supported in part by the NSF grant 1204944 at the University of Minnesota. The research of JS has been supported at IAP by the ERC project 267117 (DARK) hosted by Université Pierre et Marie Curie - Paris 6, PI: JS. JS also acknowledges the support of the JHU by NSF grant OIA-1124403,

REFERENCES

Atek H. et al., 2014, preprint (arXiv:1409.0512)
Bazin G. et al., 2009, A&A, 499, 653
Behroozi P. S., Silk J., 2014, preprint (arXiv:1404.5299)
Behroozi P. S., Wechsler R. H., Conroy C., 2013, ApJ, 770, 57
Botticella M. T. et al., 2008, A&A, 479, 49
Bouwens R. J., Illingworth G. D., Franx M., Ford H., 2007, ApJ, 670, 928
Bouwens R. J., Illingworth G. D., Franx M., Ford H., 2008, ApJ, 686, 230
Bouwens R. J. et al., 2011, ApJ, 737, 90
Bouwens R. et al., 2014a, ApJ, 795, 126
Bouwens R. J. et al., 2014b, preprint (arXiv:1403.4295)
Bromm V., 2013, Rep. Prog. Phys., 76, 112901
Bromm V., Larson R. B., 2004, ARA&A, 42, 79
Bromm V., Loeb A., 2002, ApJ, 575, 111
Bromm V., Loeb A., 2003, Nature, 425, 812
Bromm V., Yoshida N., Hernquist L., McKee C. F., 2009, Nature, 459, 49
Burgarella D. et al., 2013, A&A, 554, A70
Chabrier G., 2003, PASP, 115, 763
Chary R., Berger E., Cowie L., 2007, ApJ, 671, 272
Chen K. J., Bromm V., Heger A., Jeon M., Woosley S., 2014, preprint (arXiv:1407.7545)
Connolly A. J., Szalay A. S., Dickenson M., SubbaRao M. U., Brunner R. J., 1997, ApJ, 486, L11
Cucchiara A., Fumagalli M., Rafelski M., Kocevski D., Prochaska J. X., Cooke R. J., Becker G. D., 2014, preprint (arXiv:1408.3578)
Daddi E. et al., 2007, ApJ, 670, 156
Dahlen T., Strolger L.-G., Riess A. G., Mattila S., Kankare E., Mobasher B., 2012, ApJ, 757, 70
Daigne F., Olive K. A., Vangioni-Flam E., Silk J., Audouze J., 2004, ApJ, 617, 693
Daigne F., Rossi E. M., Mochkovitch R., 2006a, MNRAS, 372, 1024
Daigne F., Olive K. A., Silk J., Stoehr F., Vangioni E., 2006b, ApJ, 647, 773
Damen M., Labbé I., Franx M., van Dokkum P. G., Taylor E. N., Gawiser E. J., 2009, ApJ, 690, 937
Duncan K. et al., 2014, MNRAS, 444, 2960
Finkelstein S. L. et al., 2012, ApJ, 756, 164
Frebel A., Norris J. E., 2013, in Oswalt T. D., Gilmore G., eds, Planets, Stars and Stellar Systems Vol. 5: Galactic Structure and Stellar Populations. Springer-Verlag, Dordrecht, p. 55
Frebel A., Johnson J. L., Bromm V., 2007, MNRAS, 380, L40
Gallerani S., Salvaterra R., Ferrara A., Choudhury T. R., 2008, MNRAS, 388, L84
Genel S. et al., 2014, MNRAS, 445, 175
González V., Bouwens R., Illingworth G., Labb I., Oesch P., Franx M., Magee D., 2014, ApJ, 781, 34
Graur O. et al., 2011, MNRAS, 417, 916
Greif T. H., Bromm V., 2006, MNRAS, 373, 128
Heger A., Woosley S. E., 2010, ApJ, 724, 341
Hinshaw G. et al., 2013, ApJS, 208, 19
Hjorth J. et al., 2003, Nature, 423, 847
Hopkins A. M., 2004, ApJ, 615, 209
Hopkins A. M., Beacom J. F., 2006, ApJ, 651, 142
Ishida E. E. O., de Souza R. S., Ferrara A., 2011, MNRAS, 418, 500
Jimenez R., Piran T., 2013, ApJ, 773, 126
Kistler M. D., Yüksel H., Beacom J. F., Stanek K. Z., 2008, ApJ, 673, L119
Kistler M. D., Yüksel H., Beacom J. F., Hopkins A. M., Wyithe J. S. B., 2009, ApJ, 705, L104
Kistler M. D., Yuksel H., Hopkins A. M., 2013, preprint (arXiv:1305.1630)
Lamb D. Q., Reichart D. E., 2000, ApJ, 536, 1
Le Borgne D., Elbaz D., Ocvirk P., Pichon C., 2009, A&A, 727, 740
Li W., Chornock R., Leaman J., Filippenko A. V., Poznanski D., Wang X., Ganeshalingam M., Mannucci F., 2011, MNRAS, 412, 1473
Lilly S. J., Le Fevre O., Hammer F., Crampton D., 1996, ApJ, 460, L1
McLure R. J. et al., 2013, MNRAS, 432, 2696
Madau P., Dickinson M., 2014, ARA&A, 52, 415
Madau P., Ferguson H. C., Dickenson M. E., Giavalisco M., Steidel C. C., Fruchter A., 1996, MNRAS, 283, 1388
Madau P., Pozzetti L., Dickinson M., 1998, ApJ, 498, 106
Mao S., Mo H. J., 1998, A&A, 339, L1
Mattila S. et al., 2012, ApJ, 756, 111
Melinder J. et al., 2011, A&A, 532, 29
Nelder J. A., Mead R., 1965, Comput. J., 7, 308
Noeske K. G. et al., 2007, ApJ, 660, L47
Oesch P. A. et al., 2012, ApJ, 759, 135
Oesch P. A. et al., 2013, ApJ, 773, 75
Oesch P. A. et al., 2014a, ApJ, 786, 108
Oesch P. A., Bouwens R. J., Illingworth G. D., Franx M., Ammons S. M., van Dokkum P. G., Trenti M., Labbe I., 2014b, preprint (arXiv:1409.1228)
Petitjean P., Ledoux C., Srianand R., 2008, A&A, 480, 349

Pettini M., Zych B. J., Steidel C. C., Chaffee F. H., 2008, MNRAS, 385, 2011
Planck Collaboration XVI, 2014, A&A, 566, 54
Planck Collaboration XVI, 2014, A&A, 571, 16
Popesso P., Biviano A., Böhringer H., Romaniello M., 2006, A&A, 445, 29
Porciani C., Madau P., 2001, ApJ, 548, 522
Press W. H., Schechter P., 1974, ApJ, 187, 425
Prochaska J. X., Wolfe A. M., 2009, ApJ, 696, 1543
Prochaska J. X., Herbert-Fort S., Wolfe A. M., 2005, ApJ, 635, 123
Rafelski M., Wolfe A. M., Prochaska J. X., Neeleman M., Mendez A. J., 2012, ApJ, 755, 89
Reddy N. A. et al., 2012, ApJ, 744, 154
Robertson B. E., Ellis R. S., 2012, ApJ, 744, 95
Robertson B. E. et al., 2013, ApJ, 768, 71
Rollinde E., Vangioni E., Maurin D., Olive K. A., Daigne F., Silk J., Vincent F. H., 2009, MNRAS, 398, 1782
Safranek-Shrader C., Bromm V., Milosavljević M., 2010, ApJ, 723, 1568
Sawicki M. J., Lin H., Yee H. K. C., 1997, AJ, 113, 1
Schaerer D., 2002, A&A, 382, 28
Schaye J. et al., 2015, MNRAS, 446, 521
Schneider R., Omukai K., 2010, MNRAS, 402, 429
Schneider R., Salvaterra R., Ferrara A., Ciardi B., 2010, MNRAS, 369, 825
Shull J. M., Harness A., Trenti M., Smith B. D., 2012, ApJ, 747, 100
Smith B. D., Turk M. J., Sigurdsson S., O'Shea B. W., Norman M. L., 2009, ApJ, 691, 441
Sokolov V. V., 2014, in Ryutin R., Petrov V., Kiselev V., eds, Proc. XXIXth Int. Workshop High Energy Phys., New Results and Actual Problems in Particle & Astroparticle Physics and Cosmology, World Scientific Press, Singapore, p. 201
Springel V., Hernquist L., 2003, MNRAS, 339, 312
Stanek K. Z. et al., 2003, ApJ, 591, L17
Stark D. P., Schenker M. A., Ellis R. S., Robertson B., McLure R., Dunlop J., 2013, ApJ, 763, 129
Steidel C. C., Giavalisco M., Pettini M., Dickinson M., Adelberger K. L., 1996, ApJ, 462, L17
Suda T. et al., 2008, PASJ, 60, 1159
Suda T., Yamada S., Katsuta Y., Komiya Y., Ishizuka C., Aoki W., Fujimoto M. Y., 2011, MNRAS, 412, 843
Tanvir N. R. et al., 2009, Nature, 461, 1254
Tornatore L., Ferrara A., Schneider R., 2007, MNRAS, 382, 945
Totani T., 1997, ApJ, 486, L71
Trenti M., Stiavelli M., Bouwens R. J., Oesch P., Shull J. M., Illingworth G. D., Bradley L. D., Carollo C. M., 2010, ApJ, 714, L202
Trenti M., Perna R., Levesque E. M., Shull J. M., Stocke J. T., 2012, ApJ, 749, L38
Trenti M., Perna R., Tacchella S., 2013, ApJ, 773, L22
Vergani S. D., 2013, in Cambresy L., Martins F., Nuss E., Palacios A., eds, PNHE worshop, SF2A meeting, Montpellier, France, Proc. Annu. Meeting French Soc. Astron. Astrophys., p. 377
Vergani S. D. et al., 2014, preprint (arXiv:1409.7064)
Wanderman D., Piran T., 2010, MNRAS, 406, 1944
Wang F. Y., 2013, A&A, 556, A90
Wang F. Y., Dai Z. G., 2009, MNRAS, 400, L10
Wang F. Y., Bromm V., Greif T. H., Stacy A., Dai Z. G., Loeb A., Cheng K. S., 2012, ApJ, 760, 27
Wijers R. A. M. J., Bloom J. S., Bagla J. S., Natarajan P., 1998, MNRAS, 294, L13
Woosley S. E., Bloom J. S., 2006, ARA&A, 44, 507
Woosley S. E., Weaver T. A., 1995, ApJS, 101, 181
Wyithe J. S. B., Hopkins A. M., Kistler M. D., Yüksel H., Beacom J. F., 2010, MNRAS, 401, 2561
Wyithe J. S. B., Loeb A., Oesch P. A., 2014, MNRAS, 439, 1326
Yoshida N., Bromm V., Hernquist L., 2004, ApJ, 605, 579
Yoshii Y., Saio H., 1986, ApJ, 301, 587
Yüksel H., Kistler M. D., Beacom J. F., Hopkins A. M., 2008, ApJ, 683, L5
Zafar T., Centurin M., Proux C., Molaro P., D'Odorico V., Vladilo G., Popping A., 2014, MNRAS, 444, 744
Zwart J. T. L., Jarvis M. J., Deane R. P., Bonfield D. G., Knowles K., Madhanpall N., Rahmani H., Smith D. J. B., 2014, MNRAS, 439, 1459

This paper has been typeset from a TEX/LATEX file prepared by the author.